Evaluation of the SIF and T-stress values of the Brazilian Disc with a Central Notch by Hybrid Method.

Authors Name and Affiliations

Petr Miarka[a,b], Alejandro Sanchez-Cruces[c], Stanislav Seitl[a,b], Lucie Malíková[a,b], Pablo Lopez-Crespo[c]

[a] Institute of Physics of Materials, Academy of Sciences of the Czech Republic, Žižkova 22, 616 62 Brno, Czech Republic

[b] Brno University of Technology, Faculty of Civil Engineering, Veveří 331/95, 602 00 Brno, Czech Republic

[c] Department of Civil and Materials Engineering, University of Malaga, C/Dr Ortiz Ramos s/n, 29071 Malaga, Spain

Corresponding Author

Petr Miarka (Petr.Miarka@vut.cz) +420 54114 7116

Abstract

The near-crack-tip displacement field of a Brazilian disc with a central notch (BDCN) under mixed mode I/II conditions was measured via digital image correlation (DIC) and the stress intensity factor (SIF) was estimated using a hybrid method that allowed the fitting of the experimental data into the Williams series expansion. The effects of higher-order terms in the Williams expansion (*T*-stress) were analysed for different sizes of the crack tip fitting region and the results were compared with analytical predictions as well as with results obtained based on the numerically calculated crack-tip displacement field.

Keywords: *T*-stress, DIC, Brazilian disc, Concrete, Mixed mode I/II.

Abbreviations/nomenclature

2D	two-dimensional
BDCN	Brazilian disc with a central notch
DIC	digital image correlation
FEA	finite element analysis
LEFM	linear elastic fracture mechanics
ODM	over-deterministic method
SIF	stress intensity factor
WE	Williams expansion
HPC	high performance concrete
β	biaxiality parameter (-)
ν	Poisson's ratio (-)
α	initial notch angle (°)
ΔX, ΔY	distance increment in the X and Y direction (mm)
f_n^I, g_n^I	known shape functions for mode I (-)
$[C]$	shape function matrix (-)
$[U]$	displacements vector (mm)
$[X]$	vector of unknown coefficients of the WE (-)
a	initial notch length (mm)
B	specimen thickness (mm)

E	Young's modulus of elasticity (GPa)
k	number of displacement values in ODM evaluation (-)
K_I	stress intensity factor for mode I (MPam$^{1/2}$)
K_II	stress intensity factor for mode II (MPam$^{1/2}$)
N,M	number of unknown coefficients of the WE (-)
P	load (kN)
R	specimen radius (mm)
r,θ	polar coordinates (mm) and (rad)
r_C	critical distance (mm)
T-stress	T-stress in the crack plane (MPa)
u	horizontal displacement (mm)
v	vertical displacement (mm)
σ_t	tensile strength (MPa)

1. Introduction

For the last decade, the design of newly built concrete structures has considered the economic and environmental impact of new structures. This has led to the development of materials which have higher mechanical performance and a lower impact on the environment. The use of high-performance concrete (HPC) [1, 2] is such an application. The production of HPC consumes much less natural resources (i.e. raw materials for cement, aggregates and water) than standard concrete, and the mixture itself contains less cement (lower CO_2 production), while improved mechanical properties allow the production cost (thin walled structural elements) to be reduced.

To reduce the natural resources used and improve the mechanical characteristics of concrete mixture, mineral admixtures are added to the HPC mixture, i.e. secondary pozzolans like silica fume [3], high furnace slag [4], fly ash, etc. HPC is used where the weight reduction of a structure is crucial or where the architectural design demands smaller and thinner load-bearing structural elements for a required aesthetic value. However, these demands can lead to easier crack initiation and propagation.

Typically, tensile mode I crack opening and propagation are studied, while shear mode II is normally neglected in most research works. Even a simply supported beam with distributed load (see Figure 1(a)) carries such a combination of mode I and mode II load. If the stress distribution is plotted in principal stresses, one can find the location of the highest tensile mode I stresses and highest mode II shear stresses, which produce the main failure mechanism (transverse tension) of concrete structures. Nevertheless, there is a location with a combination of tensile and shear stress which produces mixed mode I/II crack initiation. This fact is unintentionally omitted in studies, and in practice this weakest material point is strengthened using shear reinforcement – stirrups [5] (see Figure 1(b)). However, static or cyclic load [6, 7] can lead to microcracks in the concrete cover layer which propagate and increase in size until final failure occurs [8, 9]. This often leads to reinforcement exposure, and thus to the reduction of the total service lifetime [10-12].

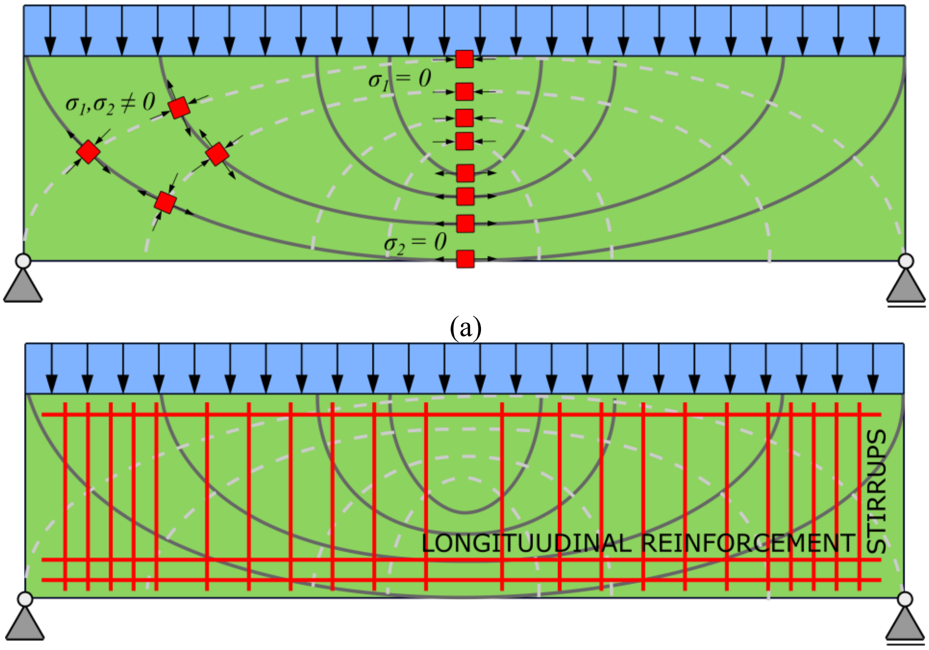

(a)

(b)

Figure 1: Illustrative principal stress distributions (a) and reinforcement (b) of a simply supported beam with a distributed load.

Usually, mixed mode I/II fracture is studied via various crack initiation criteria, e.g. the maximum tangential stress (MTS) criterion [13], the strain energy density (SED) criterion[14], the generalized maximum tangential stress (GMTS) criterion [15], the generalised strain energy density (GSED) criterion [16], and others. The first two criteria consider the stress intensity factor (SIF) for mode I and mode II, while the GMTS criterion uses SIFs, the T-stress and the critical distance r_C in the calculation of the crack initiation direction under mixed mode I/II. The SIFs and T-stress can be evaluated directly using the Williams expansion (WE) postulated by Williams [17], or (for some simple configurations) expressed explicitly from an analytical solution. They are summed up in various handbooks [18, 19] and extensively studied by Atkinson [20]. Experimental verification of the analytical formulations mentioned in handbooks can be done by employing the digital image correlation (DIC) method [21, 22], which captures the displacement fields that arise during experimental testing. The aim of this experimental study is to investigate various displacement fields in the close vicinity of the crack tip measured under various loading mode mixity conditions. For this, a Brazilian disc with a central notch (BDCN) was used, see Figure 33 The used BDCN specimen was made from HPC and the initial notch had two different lengths, which produce different mode mixities and constraint levels. The displacement field was captured via DIC measurement and compared with a displacement field generated numerically by means of finite element analysis (FEA). Both of these displacements were arranged as an input to the over-deterministic method (ODM) [23], which provides a relatively simple solution of the WE terms. The evaluated values for K_I, K_{II} and T-stress were compared with data found in the literature.

2. Theoretical Background

First, the Williams expansion for the description of stress and displacement fields in a cracked body under mixed mode I/II conditions is presented. Then we describe the formula used for the SIFs and T-stress calculation. Finally, we briefly discuss the over-deterministic method used in the evaluation of the experimental data.

2.1 Stress and Displacement Fields for Mixed Mode I/II

This experimental study is based on the linear elastic fracture mechanics (LEFM) concept. LEFM uses the WE for the description of the stress fields in the close vicinity of the tip of a crack in homogeneous isotropic cracked material. The Cartesian/polar coordinate system is used for the description of stress and displacement fields, as shown in Figure 22.

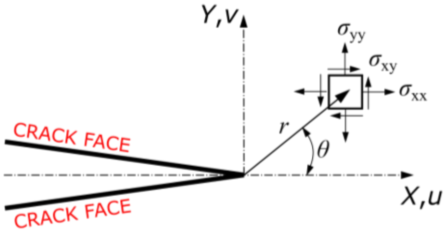

Figure 2: Coordinate system and related stress components.

This expansion is an infinite power series which describes the stress field as follows:

$$\begin{Bmatrix}\sigma_{xx}\\ \sigma_{yy}\\ \sigma_{xy}\end{Bmatrix} = \sum_{n=1}^{\infty}\frac{n}{2}A_n r^{\left(\frac{n}{2}-1\right)}\begin{Bmatrix}\left(2+\frac{n}{2}+(-1)^n\right)cos\left(\frac{n}{2}-1\right)\theta-\left(\frac{n}{2}-1\right)cos\left(\frac{n}{2}-3\right)\theta\\ \left(2-\frac{n}{2}-(-1)^n\right)cos\left(\frac{n}{2}-1\right)\theta+\left(\frac{n}{2}-1\right)cos\left(\frac{n}{2}-3\right)\theta\\ \left(\frac{n}{2}-1\right)sin\left(\frac{n}{2}-3\right)\theta-\left(\frac{n}{2}+(-1)^n\right)sin\left(\frac{n}{2}-1\right)\theta\end{Bmatrix}$$

$$-\sum_{n=1}^{\infty}\frac{n}{2}B_n r^{\left(\frac{n}{2}-1\right)}\begin{Bmatrix}\left(2+\frac{n}{2}-(-1)^n\right)sin\left(\frac{n}{2}-1\right)\theta-\left(\frac{n}{2}-1\right)sin\left(\frac{n}{2}-3\right)\theta\\ \left(2-\frac{n}{2}+(-1)^n\right)sin\left(\frac{n}{2}-1\right)\theta+\left(\frac{n}{2}-1\right)sin\left(\frac{n}{2}-3\right)\theta\\ -\left(\frac{n}{2}-1\right)cos\left(\frac{n}{2}-3\right)\theta+\left(\frac{n}{2}-(-1)^n\right)cos\left(\frac{n}{2}-1\right)\theta\end{Bmatrix}, \tag{1}$$

where *r* and *θ* are the polar coordinates, *n* is the order of the term in the infinite power series, coefficient A_n corresponds to mode I and coefficient B_n corresponds to mode II. The coefficient of the first singular term for $n = 1$, i.e. A_1, is related to the stress intensity factor for mode I, and the second coefficient A_2 corresponds to the distance-independent term called *T*-stress. For mode II the first singular term for $n = 1$, i.e. B_1, is related to the stress intensity factor for mode II. These terms can be calculated as follows:

$$K_I = \sqrt{2\pi}A_1;\ T = 4A_2, K_{II} = -\sqrt{2\pi}B_1. \tag{2}$$

As with the stresses, the displacement field around the crack tip can be expressed using the WE:

$$\begin{aligned} u = &\sum_{n=0}^{N}\frac{A_n}{2\mu}r^{\frac{n}{2}}\left\{\left(\kappa+\frac{n}{2}+(-1)^n\right)cos\frac{n}{2}\theta-\frac{n}{2}cos\left(\frac{n}{2}-2\right)\theta\right\}\\ &+\sum_{n=0}^{M}\frac{B_n}{2\mu}r^{\frac{n}{2}}\left\{\left(-\kappa-\frac{n}{2}+(-1)^n\right)sin\frac{n}{2}\theta+\frac{n}{2}sin\left(\frac{n}{2}-2\right)\theta\right\}\\ &= f_0A_0+\sum_{n=1}^{N}A_nf_n^I(r,\theta)\ +\sum_{n=0}^{M}B_nf_n^{II}(r,\theta)\,, \end{aligned} \tag{3}$$

$$\begin{aligned} v = &\sum_{n=0}^{N}\frac{A_n}{2\mu}r^{\frac{n}{2}}\left\{\left(\kappa-\frac{n}{2}-(-1)^n\right)sin\frac{n}{2}\theta-\frac{n}{2}sin\left(\frac{n}{2}-2\right)\theta\right\}\\ &+\sum_{n=0}^{M}\frac{B_n}{2\mu}r^{\frac{n}{2}}\left\{\left(\kappa-\frac{n}{2}+(-1)^n\right)cos\frac{n}{2}\theta+\frac{n}{2}cos\left(\frac{n}{2}-2\right)\theta\right\}\\ &= g_0B_0+\sum_{n=0}^{N}A_ng_n^I(r,\theta)+\sum_{n=1}^{M}B_ng_n^{II}(r,\theta)\,. \end{aligned} \tag{4}$$

In Eqs. 3-4, u and v are the displacement vector components in the x and y direction, μ is the shear modulus, which can be expressed as $E/2(1 + \nu)$, κ is Kolosov's constant for plane strain $3 - 4\nu$ and for plane stress $(3 - \nu)/(1 + \nu)$ conditions, and E and ν are the Young's modulus and the Poisson's ratio, respectively. $f_n^I(r,\theta)$ and $g_n^I(r,\theta)$ are known geometry functions for mode I and $f_n^{II}(r,\theta)$ and $g_n^{II}(r,\theta)$ are known geometry functions for mode II in polar coordinates. The terms f_0A_0 and g_0B_0 are the displacements corresponding to $n = 0$ and are directly related to the rigid body translation of the crack tip.

2.2 The Stress Intensity Factor for Mixed Mode I/II and *T*-stress

A BDCN specimen was used due to the simplicity of specimen preparation, the relatively simple experimental setup and the possibility of mixed mode I/II loading. This loading is achieved by inclining the initial notch to the loading point at the angle α. A diagram of the BDCN specimen is presented in Figure 3.

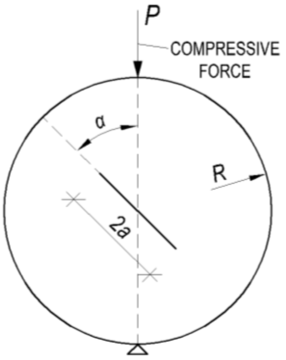

Figure 3: Dimensions and boundary conditions of a Brazilian disc with a central notch (BDCN).

The SIFs for mode I and mode II are calculated using Eqs. 5-6 according to the handbook by Tada & Paris [18].

$$K_I = \frac{P\sqrt{a}}{RB\sqrt{\pi}} \frac{1}{\sqrt{1-\frac{a}{R}}} Y_I(a/R, \alpha), \tag{5}$$

$$K_{II} = \frac{P\sqrt{a}}{RB\sqrt{\pi}} \frac{1}{\sqrt{1-\frac{a}{R}}} Y_{II}(a/R, \alpha), \tag{6}$$

where P is the applied compressive load, R is the specimen radius, a is the crack length, α is the notch inclination angle, B is the thickness of the specimen and Y_{I} and Y_{II} are the shape functions for mode I and mode II, respectively. The values of the shape functions for mode I and mode II can be found in the literature, e.g. Ayatollahi Aliha [24], Seitl [25] et al. and Fett [26]. In this study, two different notch lengths a/R were chosen, which results in different values being obtained for SIF and the level of constraint. The difference in SIF values is shown in Figure 4(a), while Figure 4(b) shows the difference for *T*-stress.

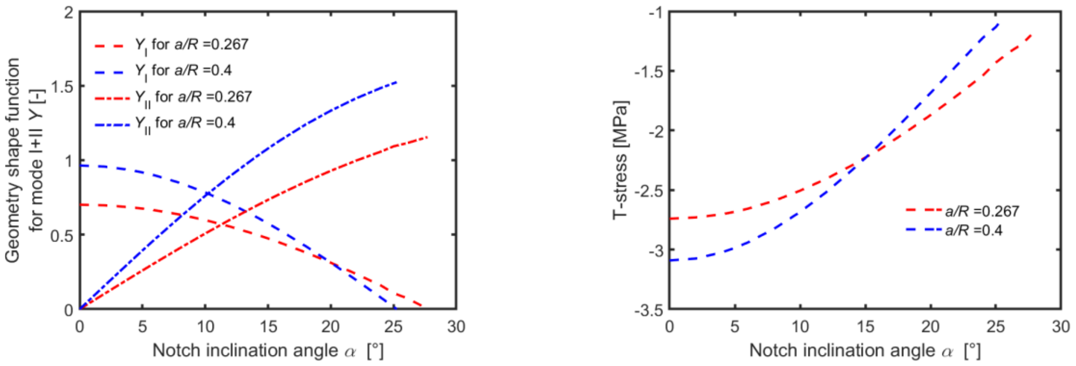

(a) (b)

Figure 4: Comparison of the differences between the SIF (a) and *T*-stress (b) values for two different notch lengths.

Various solutions for the evaluation of the elastic *T*-stress can be found in works by Leevers and Radon [27], Knesl and Bednar [28], and Fett [26]. All of these authors proposed the following relation between the biaxiality parameter β, mode I stress intensity factor K_I, *T*-stress T and crack length a:

$$\beta = \frac{T\sqrt{\pi a}}{K_I} \ . \qquad (7)$$

Based on the biaxiality parameter values presented in the mentioned handbooks, the *T*-stress can be obtained for basic cracked specimens. However, for the BDCN specimen, the K_I values for some angles α can be equal to zero, which leads to infinite values of β. For this reason, it is recommended that another method be used, i.e. the direct extrapolation method [29], or that finite element software be used to directly obtain the *T*-stress value.

2.3 The Over-Deterministic Method

To evaluate the SIFs and *T*-stress derived from the Williams expansion, the over-deterministic method (ODM) proposed by Ayatollahi and Nejati [23] can be used. This is an improvement of the general method proposed by Sanford and Dally [30], which also determines SIFs and far field stress from displacement, does not account for higher order terms of the WE. The current implementation of ODM generated reliable results previously [31].The ODM utilizes k numbers of horizontal u and vertical v displacements of the displacement fields. Using Eqs. 3 and 4, where the unknowns are only N numbers of A_n coefficients and M numbers of B_n coefficients, an over-determined system of equations can be formed:

$$[U]_{2k+1} = [C]_{2k\times(N+M+2)}[X]_{(N+M+2)}, \qquad (8)$$

where $[U]$ contains the displacements u and v, $[C]$ contains the values of shape functions $f_I(r,\theta)$ and $g_I(r,\theta)$ for mode I and shape functions $f_{II}(r,\theta)$ and $g_{II}(r,\theta)$ for mode II, $[X]$ are the unknown WE coefficients and N and M are the demanded number of evaluated WE coefficients. This leads to the solution by the least-square method in a vector form expressed as:

$$[X] = ([C]^T[C])^{-1}[C]^T[U]. \qquad (9)$$

3. Experimental Details

First, we introduce the material used within the study together with the measured material's mechanical properties. Then the specimen's geometry is presented. Afterwards, we present the digital image correlation technique which was used in the measurement of displacement fields in front of the notch tip. Lastly, the experimental set-up for the BDCN specimen is introduced.

3.1 Material

High strength concrete was designed with the intent to produce thinner and lighter precast concrete structural elements. The aggregates were composed from natural sand 0/4 mm and crushed high quality granite 4/8 mm (the maximum aggregate size is 8 mm). Portland cement CEM I 42.5 R was used with three mineral admixtures, see [32]. Generally, binder consists of 81 % CEM I 42.5 R, 9.5 % metakaolin, 7.5 % GBFS and 2.5 % limestone. The water/binder ratio was 0.22. A polycarboxylate-based superplasticizer was selected with regard to its compatibility with cement. The concrete was mixed in a volume of 0.7 m^3 and poured into moulds.

The mechanical properties of the studied HPC were measured in accordance with European standards at 28 days and are presented in Table 1.

Table 1: Mechanical parameters (with their standard deviations) of the studied HPC at 28 days.

Compressive strength $f_{c,cube}$ [MPa]	106.2 ± 2.5
Young's modulus E [GPa]	41.0 ± 0.6
Flexural strength f_{ct} [MPa]	9.3 ± 0.9
Indirect tensile strength f_t [MPa]	6.43 ± 0.3

The concrete was tested at the age of 1 day and 28 days, while some other characteristics – especially non-destructive - were tested at a later age. Due to the mixing of the concrete in the industrial mixer, the mechanical properties, especially compressive strengths, were lower compared to those from laboratory tests. The measured mechanical properties from the tests were as follows: the 150 mm cube compressive strength was (65.2 ± 1.4) MPa at the age of 24 hours and (106.2 ± 2.5) MPa at 28 days, while the flexural strength at the age of 28 days was (9.3 ± 0.9) MPa and the static modulus of elasticity measured on cylinders of 150 mm × 300 mm was (41.0 ± 0.6) GPa. However, the measured/calculated values of E were lower than expected with respect to compressive strength – the absence of coarse aggregates could be a reason [33].

Basic fracture properties can be tested on various types of specimen, and various methods for the assessment of results have been published, see e.g. [34-36].For the purposes of this work, the fracture mechanical properties of notched beams and a BDCN specimen were tested. The beams had dimensions of 80 mm × 80 mm × 480 mm in accordance with Karihaloo's and Nallathambi's effective crack model [34], afterwards test were carried out on a BDCN specimen. The FMPs measured from the beams were: modulus of elasticity $E = 46.5\pm1.2$ GPa, which is similar to the values from the mechanical measurements, see Table 1; effective crack length $a_{ef} = 15.5\pm2.8$ mm; effective fracture toughness $K_{ICe} = 1.74\pm0.18$ MPam$^{1/2}$ and fracture energy $G_C = 65\pm11$ Jm^{-2}. The evaluated fracture toughness value from the BDCN specimen test is $K_{IC,BDCN} = 1.106\pm0.06$ MPa m$^{1/2}$. This result is 45% lower than the K_{IC} measured on the geometry of notched beams. The difference is caused by the geometry effect. This geometry effect was recently discussed for limestone in [37] and for concrete in [25].

3.2 Specimen Geometry

In this experimental study, a BDCN specimen was tested with two different notch lengths and various notch inclination angles α. The BDCN specimens were manufactured from a standardized cylindrical specimen with the diameter $D = 150$ mm (radius $R = D/2$) and a thickness B of 30 mm. The initial notch was made by a water jet cutter in order to provide a straight-through notch. The initial notch lengths $2a$ were 40 and 60 mm, respectively. These specimens were tested under mixed mode I/II load conditions and for the pure mode II, which is performed by varying the notch inclination angle α (please note that the angle corresponding to the pure mode II varies based on the selected a/R ratio).

The actual measured dimensions of D, B and a are presented in Table 2.

Table 2: Measured dimensions of the used Brazilian disc specimens.

Specimen	*α* [°]	*D* [mm]	*B* [mm]	2*a* [mm]	*a/R* [-]
HPC_4_3_2	5	149.18	30.65	40.46	0.271
HPC_4_3_3	10	149.23	30.47	40.08	0.269
HPC_4_3_4	27.7	149.21	31.50	40.41	0.271
HPC_6_3_1	0	149.18	30.56	60.59	0.406
HPC_6_3_2	5	149.23	30.48	60.21	0.403
HPC_6_3_3	15	149.17	30.56	60.29	0.404

The dimensions of the BDCN specimen are presented in Figure 3. Real BDCN specimens with a relative notch ratio $a/R = 0.267$ are presented in Figure 5.

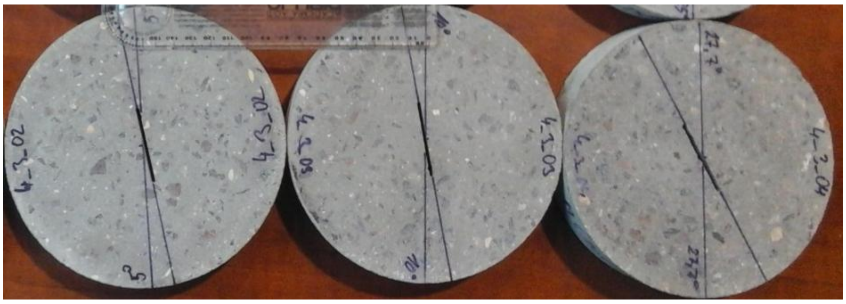

Figure 5: BDCN specimens with marked notch inclination angles with relative notch lengths *a*/*R* of 0.267.

3.3 Digital Image Correlation (DIC)

DIC was used to investigate the crack tip behaviour of the BDCN specimen for various crack lengths and various inclination angles α (see Table 3). DIC provides full-field displacement information by comparing images taken before and after straining the specimen body [38]. Each image is divided into smaller regions, or ‘interrogation windows’. The cross-correlation product is used to measure the similarity between the interrogation windows before and after straining the body for the purposes of the study:

$$c(u,v) = \sum_{x=-\frac{N}{2}}^{x=\frac{N}{2}} \sum_{y=-\frac{N}{2}}^{y=\frac{N}{2}} I_A(x,y) \cdot I_B(x+u, y+v), \tag{10}$$

where c is the cross-correlation product, which is a function of u and v, these being the displacement vectors joining the centres of the two regions of interest along directions x and y, respectively; I_A and I_B are the intensity distribution of the two digital images before and after straining the sample, respectively; and N is the number of interrogation windows into which the digital images were divided. The maximum value of the cross-correlation product (Eq. 10) is the probable displacement vector for the centre of each interrogation window in I_A. The camera was tilted so that the positive x coordinate matched the direction of crack growth and the y coordinate matched the crack opening direction. Accordingly, the angle of camera tilt was changed for the different angles α studied (Table 2). This improves the resolution of the analysis and makes post-processing easier and faster [39, 40]. DIC requires the surface to have a random pattern so that each interrogation window is unique in each image and can be located easily in the same image after it has undergone some deformation or rigid body movement. In this work, the pattern with a random grey intensity distribution was obtained by spray painting the surface with black and white speckles. An 8-bit 2048 × 2048 pixel CCD camera (Gazelle GZL-CL-41C6M) with a maximum image acquisition rate of 150 frames per second was used for taking images, and recommendations from previous analyses were followed [41]. The experimental setup was similar to the one used previously [42]. DIC generated a pair of matrices, u and v, with displacement values that were combined with an analytical model to infer fracture mechanical parameters (see the next section).

3.4 DIC data extraction

It is recognized that plastic deformation will occur at the crack tip as a result of the high stresses that are generated by the sharp stress concentration. To estimate the extent of this plastic deformation, Irwin equated the yield strength to the *Y*-direction stress along the *X*-axis and solved it for the radius. The radius value determined was the distance along the *X*-axis where the stress perpendicular to the crack direction would equal the yield strength; thus, Irwin[43] found that the extent of plastic deformation (critical distance r_C) was [44].

$$r_c = \frac{1}{2\pi}\left(\frac{K_{IC}}{\sigma_t}\right)^2 \text{ – plane stress,} \tag{11}$$

$$r_c = \frac{1}{6\pi}\left(\frac{K_{IC}}{\sigma_t}\right)^2 \text{ – plane strain.} \tag{12}$$

In Eqs. 11 and 12 K_{IC} is the fracture toughness for mode I and σ_t is the tensile strength.

To evaluate the SIFs and the *T*-stress a displacement field measured by DIC in front of the crack tip was chosen at various distances from the crack tip. The displacements were chosen outside of the critical distance, whose radius/size r_c can be evaluated by Eqs. 11 or 12. The estimated critical distance was an r_C of 1.56 mm for the plane strain and 4.67 mm for the plane stress. The calculated critical distance values justify the use of the LEFM concept, and especially the use of the WE.

Although the digital image correlation method uses a grid with a constant increment ΔX, ΔY in both directions *X* and *Y*, the numerical evaluation uses a grid in polar coordinates. The difference between the used grids is presented in Figure 6.

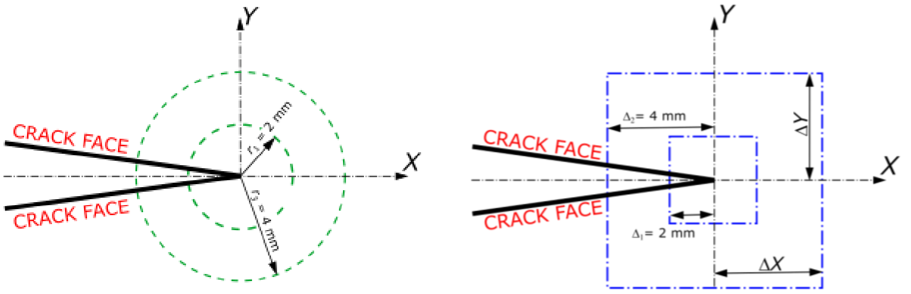

(a) (b)

Figure 6: Schema of the points whose displacements were used for the evaluation of the WE terms via the combination of the ODM and: (a) FEA; (b) DIC.

In this study, two different ΔX, ΔY distances of 2 and 4 mm for the extraction of the DIC's displacement were selected in order to fulfil the above-mentioned condition of avoiding the plastic zone around the crack tip. As in the case of the DIC measurement, a radius *r* of 2 and 4 mm were selected in order to verify the accuracy of experimentally measured displacements with data generated by the FEA. Sobel's algorithm, implemented in the edge-finding routine in the MATLAB image processing toolbox [45], was used for the determination of the crack tip position. Sobel's routine is often used for image processing analysis. It works by comparing values within a 2D displacement map. It gives a value of 1 in the regions where there is a significant discontinuity, and a value of 0 elsewhere. The edge is then located along the positions where a value of 1 was obtained. The crack is identified along the points where an edge was detected, and the crack tip is located at the end of the identified crack. This approach was previously used in fatigue and fracture applications [46, 47]. An interesting comparison of different methods for locating the crack tip from DIC maps [48] is also available. To the authors' knowledge, this is the first time that such a procedure has been applied to concrete. We are currently working on adapting the procedure for the automatic evaluation of crack tip position in composite materials [49].

Typical horizontal displacement fields *u* and vertical displacements *v* with marked crack tip locations and locations for displacement extraction are shown in Figure 7.

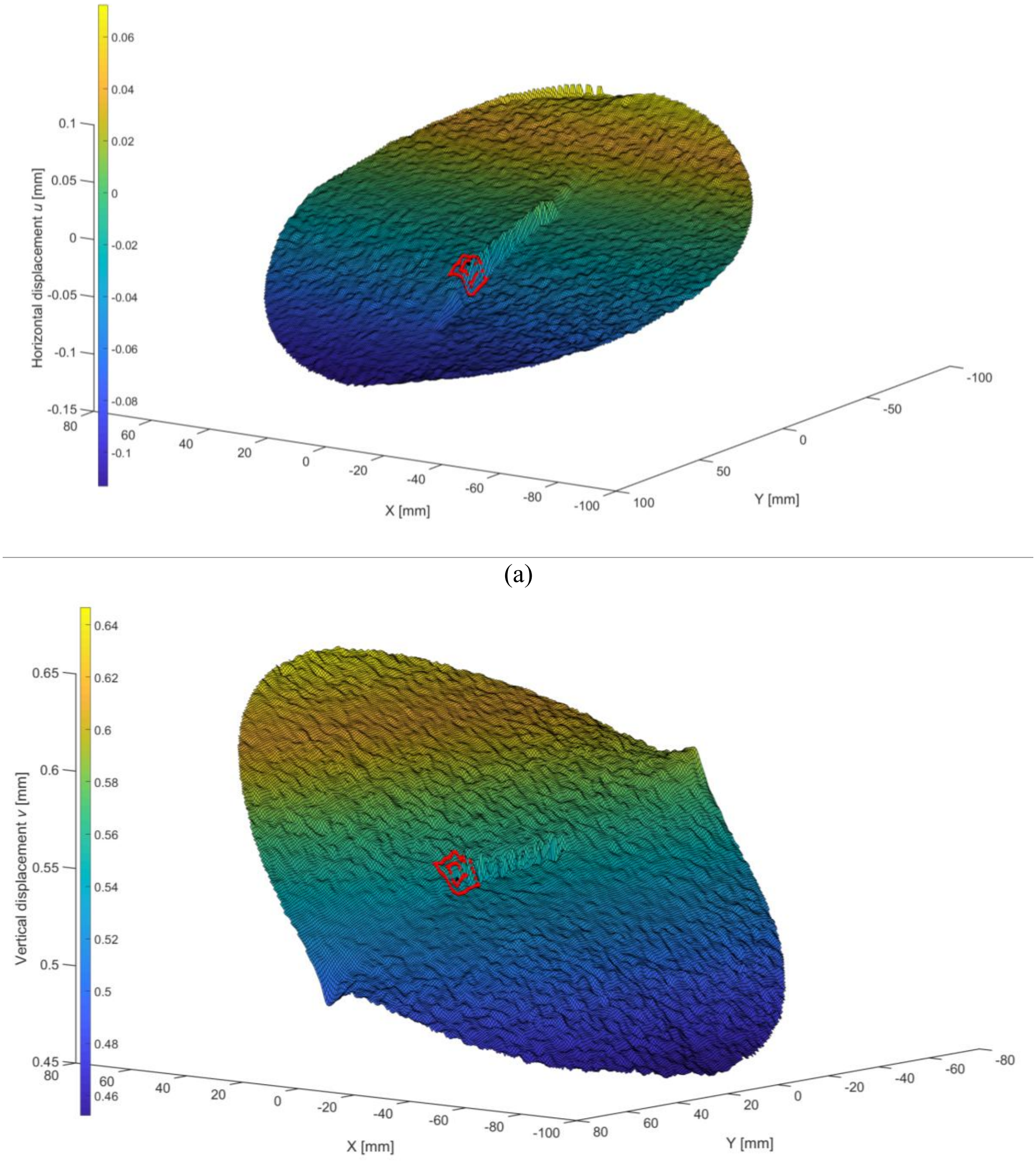

(a)

(b)

Figure 7: Displacement fields measured via the DIC technique with a marked notch tip and the chosen distance for the evaluation of the WE coefficients (a) – horizontal displacement *u* and (b) – vertical displacement *v*.

Figure 7 shows both the horizontal (Figure 7(a)) and vertical (Figure 7(b)) displacement maps collected around the crack. The slight non-symmetry observed in both maps is indicative of mode II deformation measured in the neighbourhood of the crack. Such mode II deformation plays a key role in the onset of fracture and has a major influence on the acquired results. The discontinuity generated by the crack can be observed in Figure 7(a) and 7(b) running parallel to the Y axis. Such a discontinuity was detected by Sobel's edge-finding routine and was used to estimate the crack tip position following the strategy previously described [40].

3.5 Experimental Test Setup

In this subsection, the equipment used for testing and the experimental methods are described. The experimental testing was performed on a BDCN specimen using an MTS servo-hydraulic rig with a maximum capacity of 100 kN and a vertical displacement speed of 0.01 mm/s. This experimental setup was equipped with a 4.1 MP CCD camera coupled with a Schneider lens, which provided a field of view (FOV) of 181.24 × 181.24 mm^2. Two light sources were used to ensure good homogeneous light conditions for the digital image correlation technique. The digital images were processed by VIC 2D V6 software in order to obtain a displacement field [50]. The used experimental setup is presented in Figure 8.

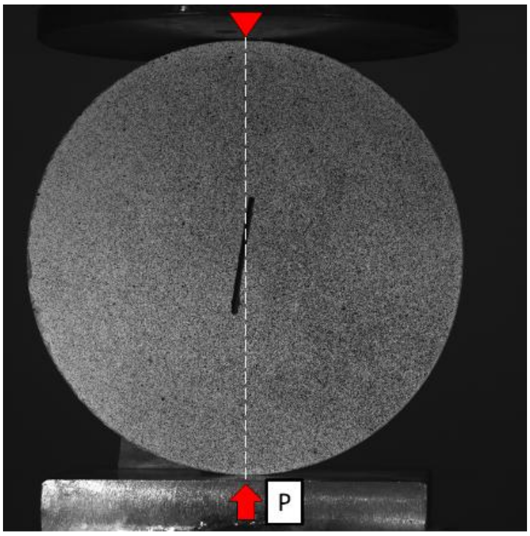

Figure 8: Experimental setup for a BDCN specimen with a treated surface for digital image correlation measurement.

The measured maximum load for various relative notch lengths a/R and various notch inclination angles are presented in Table 3.

Table 3: Maximum loading force values during the experiment for different BDCN specimens.

	a/R = 0.267		
Specimen No.	HPC_4_3_2	HPC_4_3_3	HPC_4_3_4
Notch inclination angle α [°]	5	10	27.7
Force P_{max} [kN]	22.5	24.3	27.4
	a/R = 0.4		
Specimen No.	HPC_6_3_1	HPC_6_3_2	HPC_6_3_3
Notch inclination angle α [°]	0	5	15
Force P_{max} [kN]	13.09	18.01	17.22

4. Numerical Model

In order to assess the relevance of the displacement measured by the DIC technique, a two-dimensional (2D) numerical model was created in a finite element analysis (FEA) software ANSYS [51]. The numerical model of the BDCN specimen had the dimensions mentioned in Figure 5(a) and the material model is considered to be linear elastic. The full BDCN specimen was modelled due to the presence of mode II deformations.

The input material parameters were a Young's modulus E of 41 GPa and a Poisson's ratio ν of 0.2. The model was meshed with quadrilateral 8-node elements (PLANE183) with plane strain conditions (see Figure 9(a)). The crack tip was meshed using the KSCON command in order to take into account the crack tip singularity and to provide angularly structured mesh. The KSCON command deforms the original quadratic elements around the crack tip into triangular ones and shifts the mid-side nodes to a distance of ¼ of the element's edge (towards the crack tip) [51]. The notch tip refinement is presented in Figure 9(b).

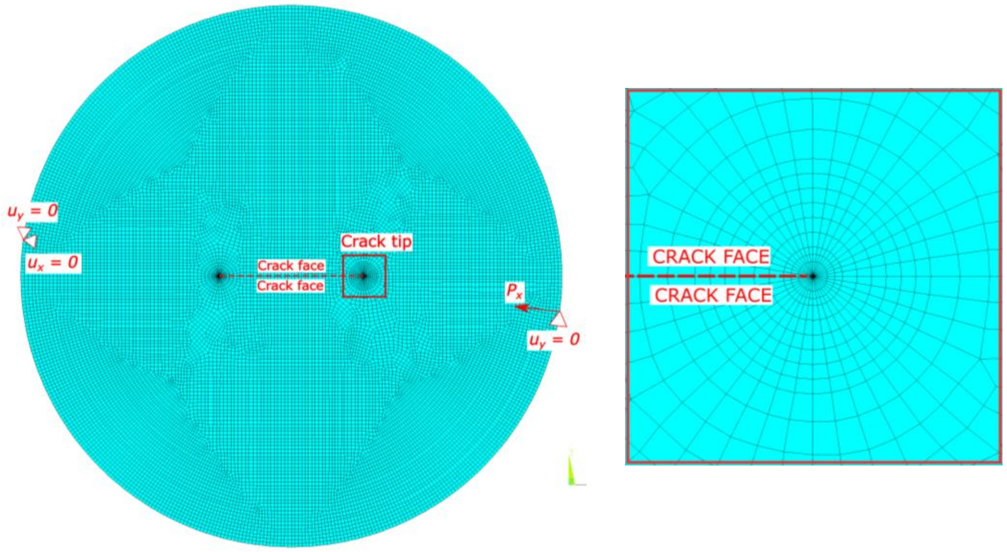

(a) (b)

Figure 9: Meshed numerical model with applied boundary conditions (a) and a detail of the crack tip refinement (b).

The model was loaded with the force P at the right edge of the disc, while the left edge was considered as a rigid support (u_x and $u_y = 0$). Adequate boundary conditions were added to prevent translation of the rigid body (see Figure 9(a)). The values of P are presented in Table 3 for each crack length.

An interaction integral [52] (which is a derivation of the J-integral [53]) is implemented in the employed FEM software. It provides a sufficient calculation of the SIF and T-stress. This calculation uses a path-independent integral around the notch at various radial distances. It is recommended that use be made of at least four different radial distances for which an interaction integral is calculated. The result is then the average value of the SIFs over these distances. The interaction integral has the following form:

$$I = \frac{2}{E^*}\left(K_1 K_1^{aux} + K_2 K_2^{aux}\right) + \frac{1}{\mu} K_3 K_3^{aux}, \tag{13}$$

where K_i is the stress intensity factor for mode I, II and III, K_1^{aux} is the auxiliary stress intensity factor for mode I, II and III, E^* is the Young's modulus for plane strain $E/(1-\nu^2)$, ν is the Poisson's ratio and μ is the shear modulus. For a 2D problem the SIF for mode III K_3 is 0. The T-stress is then calculated using the following equation:

$$T = \frac{E}{(1-\upsilon^2)}\left\{\frac{I}{f} + \upsilon \varepsilon_{33}\right\}, \tag{14}$$

where I is the interaction integral from Eq. 13, f is the line load applied along the crack front (typically $f = 1$) and ε_{33} is the extensional strain at the crack front in the direction tangential to the crack front. Both the SIFs and the T-stress are calculated as an average of four contours around the crack tip.

The mesh with refinements around the crack mentioned above is then used to extract the numerically generated nodal displacements at the demanded radial distance (ring) from the crack tip. These nodal displacements serve as input data for the ODM calculation of SIFs and T-stress. This procedure was chosen in order to verify the relevance of the calculated SIF and T-stress values, for which the optically measured displacements served as the input data.

5. Results and Discussion

In what follows, the values of the WE terms calculated based on the experimentally obtained displacement fields for the selected fatigue crack lengths are presented. Subsequently, the influence of the constraint level on the fatigue crack growth rate is evaluated and discussed.

5.1 Williams Expansion Coefficients

As mentioned above, the focus of this study was the evaluation of the SIF values, T-stress values and higher order terms of the WE. All these values were calculated for selected crack lengths.

First, we calculated the SIF values using the analytical expression stated in Eqs. 5-6 for the maximum loading force P_{max} under various mixed mode I/II loading conditions. Afterwards, we used this maximum force as an input for FEA as a first verification of the FEA model. The SIF values were calculated by means of Eq. 13. The compared results of the evaluated SIF values are presented in Table 5 for $a/R = 0.267$.

Table 4: Comparison of the SIF values calculated by the analytical formula and by FEA for the relative crack length ratio $a/R = 0.267$.

	$a/R = 0.267$		
Specimen No.	HPC_4_3_2	HPC_4_3_3	HPC_4_3_4
Notch inclination angle α [°]	5	10	27.7
Force P_{max} [kN]	22.5	24.3	27.4
K_{I} – FEA [MPam$^{1/2}$]	0.834	0.803	0.048
K_{I} – [24] [MPam$^{1/2}$]	0.625	0.597	0
K_{II} – FEA [MPam$^{1/2}$]	0.3223	0.687	1.675
K_{II} – [24] [MPam$^{1/2}$]	0.240	0.507	1.642

A similar set of results, but for the specimens with a relative notch length a/R of 0.4, is presented in Table 5.

Table 5: Comparison of SIF values calculated by the analytical formula and by the FEA for the relative crack length ratio $a/R = 0.4$.

	$a/R = 0.4$		
Specimen No.	HPC_6_3_1	HPC_6_3_2	HPC_6_3_3
Notch inclination angle α [°]	0	5	15
Force P_{max} [kN]	13.09	18.01	17.22
K_{I} – FEA [MPam$^{1/2}$]	0.3503	0.9109	0.544
K_{I} – [24] [MPam$^{1/2}$]	0.3459	0.9212	0.5515
K_{II} – FEA [MPam$^{1/2}$]	0	0.3994	1.028
K_{II} –[24] [MPam$^{1/2}$]	0.05	0.3958	1.033

In both tables, a relatively good agreement between the SIF results from the analytical solution and finite element analysis can be observed for both loading modes. The results for longer cracks exhibit better accuracy.

The experimentally obtained SIF values were compared with data found in the literature [54], where exactly the same concrete mixture was investigated. The SIF values currently obtained by employing Eqs. 5 and 6 have a similar trend to the data found in the literature, which allows further DIC measurement. The difference between the data found in the literature and that which is currently being evaluated is related to the deterioration of the concrete mixture over time and the different loading rate. A comparison is shown in Figure 10.

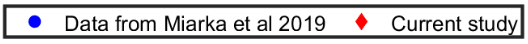

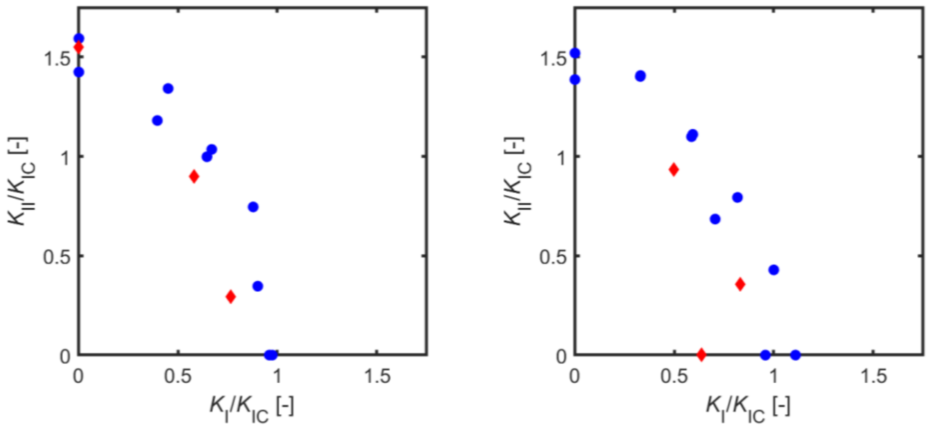

(a) (b)

Figure 10: Comparison of the currently measured SIF values (normalized via the fracture toughness) with data found in the literature – $a/R = 0.267$ (a) and $a/R = 0.4$ (b).

After verification of the material's behaviour, the ODM calculation convergence was verified for various numbers of N and M terms. The stress intensity factors were calculated from the ODM based on the numerically obtained displacement field taking into account various numbers of the initial WE terms. A comparison of the numerical SIF values calculated by means of Eq. 13 is shown in Figure 11. It was found that this method shows good agreement with the value generated by FEA with the use of more than 5 N and M terms.

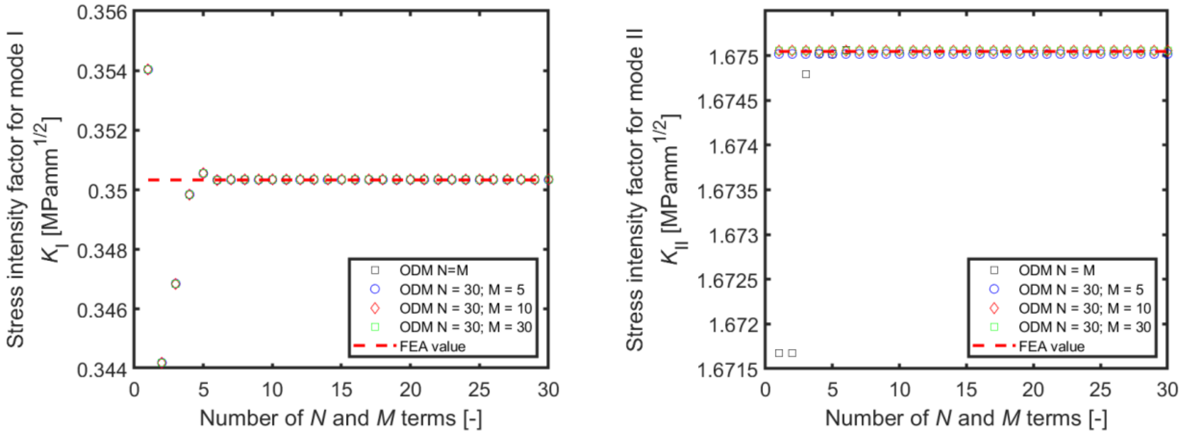

(a) (b)

Figure 11: Convergence of the evaluation of the ODM using FEA generated displacements – K_I for the pure mode I case HPC_6_3_1 specimen (a) and K_{II} for the pure mode II case HPC_4_3_4 (b).

In the next step, the displacements captured by the DIC method were used as an input for the ODM calculation. Then, a comparison with the results obtained from the ODM was performed, considering the numerically generated displacements as inputs. The results, which use DIC displacement, are K_I^{ODM} - DIC, while the results calculated using the FEA displacements are marked K_I^{ODM} – FEA. A comparison of such results for the relative crack length $a/R = 0.267$ is given in Table 6 for K_I and in Table 7 for K_{II}, respectively. Note that the results are presented again for two different radial distances from the crack tip, 2 and 4 mm.

Table 6: Comparison of K_I values generated by FEA and DIC displacement for various numbers of WE coefficients N and M for the relative notch length $a/R = 0.267$.

		$a/R = 0.267$					
Specimen No.		HPC_4_3_2		HPC_4_3_3		HPC_4_3_4	
Notch inclination angle α [°]		5		10		27.7	
r [mm]		2	4	2	4	2	4
K_I^{ODM} FEA	$N, M = 2$	0.821	0.808	0.792	0.7811	0.0576	0.0647

[MPam$^{1/2}$]	$N, M = 4$	0.837	0.832	0.802	0.8067	0.0476	0.0453
	$N, M = 10$	0.833	0.833	0.803	0.8026	0.0485	0.0485
K_I^{ODM} DIC [MPam$^{1/2}$]	$N, M = 10$	0.6291	0.7298	0.9123	0.8053	0.1148	0.0968

Table 7: Comparison of K_{II} values generated by FEA and DIC displacement for various numbers of WE coefficients N and M for the relative notch length a/R = 0.267.

		a/R = 0.267					
Specimen No.		HPC_4_3_2		HPC_4_3_3		HPC_4_3_4	
Notch inclination angle α [°]		5		10		27.7	
r [mm]		2	4	2	4	2	4
K_{II}^{ODM} FEA [MPam$^{1/2}$]	$N, M = 2$	0.3221	0.3216	0.6851	0.6838	1.6717	1.6679
	$N, M = 4$	0.3234	0.3237	0.6875	0.6862	1.6750	1.6748
	$N, M = 10$	0.3236	0.3233	0.6874	0.6866	1.6751	1.6751
K_{II}^{ODM} DIC [MPam$^{1/2}$]	$N, M = 10$	0.4822	0.5489	0.5930	0.5286	1.6408	1.6366

The results presented in Table 6 and Table 7 for DIC displacements show relatively good agreement with the SIFs obtained from FEA displacement. Of course, configurations exist for which the results correspond better (for example the deviations between the K_{II} values for the case of α = 27.7° are around 2%) than for others (for the same case of α = 27.7° the deviations between the K_I values are up to approx. 50%). This is surely connected to the high heterogeneity of the concrete specimens and the existence of a high amount of microcracks, voids or pores. As with the results performed on a/R = 0.267, a comparison for a/R = 0.4 is given in Table 8 and Table 9.

Table 8: Comparison of K_I values generated by FEA and DIC displacement for various numbers of WE coefficients N and M for the relative notch length a/R = 0.4.

		a/R = 0.4					
Specimen No.		HPC_6_3_1		HPC_6_3_2		HPC_6_3_3	
Notch inclination angle α [°]		0		5		15	
r [mm]		2	4	2	4	2	4
K_I^{ODM} FEA [MPam$^{1/2}$]	$N, M = 2$	0.34723	0.3503	0.9040	0.8968	0.5467	0.5481
	$N, M = 4$	0.3502	0.3498	0.9105	0.9093	0.5438	0.5418
	$N, M = 10$	0.3503	0.3503	0.9109	0.9109	0.5445	0.5445
K_I^{ODM} DIC [MPam$^{1/2}$]	$N, M = 10$	0.4593	0.5174	1.0142	1.0502	0.7342	0.6812

Table 9: Comparison of K_{II} values generated by FEA and DIC displacement for various numbers of WE coefficients N and M for the relative notch length a/R = 0.4.

		a/R = 0.4					
Specimen No.		HPC_6_3_1		HPC_6_3_2		HPC_6_3_3	
Notch inclination angle α [°]		0		5		15	
r [mm]		2	4	2	4	2	4
K_{II}^{ODM} FEA [MPam$^{1/2}$]	$N, M = 2$	1.034×10^{-8}	1.052×10^{-8}	0.3927	0.3916	1.0256	1.0223
	$N, M = 4$	2.223×10^{-8}	4.275×10^{-8}	0.3934	0.3931	1.0275	1.0269
	$N, M = 10$	2.746×10^{-8}	4.0712×10^{-8}	0.3935	0.3935	1.0277	1.0277
K_{II}^{ODM} DIC [MPam$^{1/2}$]	$N, M = 10$	0.0102	0.0203	0.6473	0.5713	1.1638	1.0955

The results presented in Table 8 and Table 9 show relatively good agreement, in a similar manner to the results for the relative notch length ratio a/R = 0.267. The maximum deviation is limited to a maximum of 40%. Because of the different stress distribution around the longer notch tip, which provides stable crack growth, no unambiguous trends and conclusions can be stated.

As in the case of the SIFs, the T-stress was estimated using the same abovementioned procedure. The convergence study conducted on the T-stress values showed similar results to K_I, i.e. that the T-stress converges well with the use of 5 or more mode I WE terms in the calculations. The convergence study results for the FEA study (and not the DIC data) are shown in Figure 12, while the comparison of T-stress values is shown in Table 10 and in Table 11 for both studied a/R ratios.

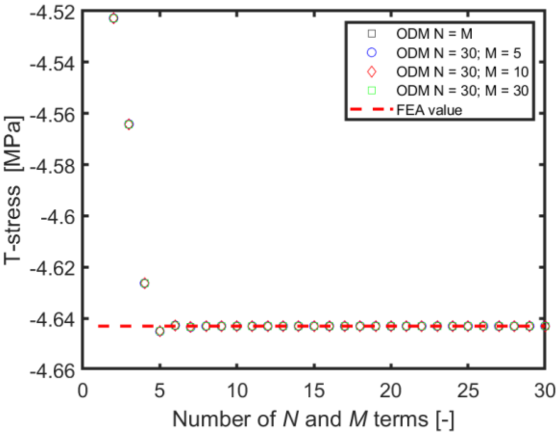

Figure 12: Convergence of the evaluation of the *T*-stress values using the ODM with FEA-generated displacements.

Table 10: Comparison of *T*-stress values generated by FEA and DIC displacement for various numbers of WE coefficients *N* and *M* for the relative notch length $a/R = 0.267$.

		$a/R = 0.267$					
Specimen No.		HPC_4_3_2		HPC_4_3_3		HPC_4_3_4	
Notch inclination angle α [°]		5		10		27.7	
r [mm]		2	4	2	4	2	4
$T\text{-}stress^{\mathrm{ODM}}$ FEA [MPa]	$N, M = 2$	-13.2335	-13.086	-13.4586	-13.3257	-7-5069	-7.5593
	$N, M = 4$	-13.5132	-13.4832	-13.6865	-13.6507	-7-2683	-7.2219
	$N, M = 10$	-13.5269	-13.5265	-13.7046	-13.7053	-7-2975	-7.2974
$T\text{-}stress^{\mathrm{ODM}}$ DIC [MPa]	$N, M = 10$	-25.4572	-20.4834	-21.6518	-22.2918	-12.5999	-6.0078

Table 11: Comparison of T-stress values generated by FEA and DIC displacement for various numbers of WE coefficients *N* and *M* for the relative notch length $a/R = 0.4$.

		$a/R = 0.4$					
Specimen No.		HPC_6_3_1		HPC_6_3_2		HPC_6_3_3	
Notch inclination angle α [°]		0		5		15	
r [mm]		2	4	2	4	2	4
$T\text{-}stress^{\mathrm{ODM}}$ FEA [MPa]	$N, M = 2$	-4.5655	-4.5228	-12.0540	-11.9507	-8.6675	-8.6543
	$N, M = 4$	-4.6382	-4.6263	-12.2154	-12.1809	-8.5943	-8.5517
	$N, M = 10$	-4.6430	-4.6430	-12.2307	-12.2308	-8.6189	-8.6189
$T\text{-}stress^{\mathrm{ODM}}$ DIC [MPa]	$N, M = 10$	-5.5649	-5.3046	-18.3196	-19.4057	-12.4568	-14.7247

The experimentally obtained results displayed in Table 10 and Table 11 show high disagreement with the values generated by FEA. This can be caused by the fact that the horizontal displacement captured by DIC showed a crack propagating from the notch tip, while the vertical displacement showed no crack propagation. This was found at the load value of $P_{\max}$ and in case of the specimens with an inclined notch, for which mode II deformations are presented. For the specimen with the pure tensile mode I ($\alpha = 0°$), this phenomenon was not observed. Therefore, the shear deformation governs the crack initiation.

6. Conclusion

Displacement fields in front of a notch tip in a Brazilian disc with a central notch specimen were investigated under various levels of mode I/II mixity. The over-deterministic method was applied in order to estimate the values of several initial coefficients of the Williams expansion derived for stress/displacement crack-tip field approximation. The values of the first two terms corresponding to the stress intensity factor and the *T*-stress were compared. This required prior identification of the crack tip location. The coordinates of the crack tip position were identified successfully with the help of a Sobel edge-finding routine. This is the first time that such a routine was applied effectively for fracture studies of concrete specimens. While the SIF values for both loading modes calculated via the ODM based on the experimentally obtained displacement field (from DIC measurements) agree well (except for in the case of some specific configurations) with the SIF values calculated via the ODM considering the numerically obtained displacement field (from FEA), the *T*-stress values obtained by both approaches differ significantly as the initial notch inclination angle increases. Thus, it can be concluded that the digital image correlation method can be reliably used for the assessment of crack behaviour in specimens where mode I prevails and/or the first singular term of the WE is dominant (typical behaviour for brittle materials where fracture occurs in the very close vicinity of the crack tip). Note that some potential deviations between the numerical and experimental results can be also connected to the high heterogeneity of the concrete specimens and the existence of a high amount of microcracks, voids or pores.

Acknowledgement

Financial support from the Czech Science Foundation (project 18-12289Y), Brno University of Technology internal grant project No. FAST-S-19-5896, and from Programa Operativo FEDER (Junta de Andalucia, Spain) through grant reference UMA18-FEDERJA-250, is gratefully acknowledged.

References

[1] P.-C. Aïtcin, R.J. Flatt, Science and technology of concrete admixtures, Woodhead publishing, 2015.
[2] E.G. Nawy, Fundamentals of High-Performance Concrete, Wiley, 2001.
[3] K.E. Hassan, J.G. Cabrera, R.S. Maliehe, The effect of mineral admixtures on the properties of high-performance concrete, Cement and Concrete Composites, 22 (2000) 267-271.
[4] R. Yu, P. Spiesz, H.J.H. Brouwers, Development of an eco-friendly Ultra-High Performance Concrete (UHPC) with efficient cement and mineral admixtures uses, Cement and Concrete Composites, 55 (2015) 383-394.
[5] C.E. De Normalisation, Eurocode 2: Design of concrete structures—Part 1-1: General rules and rules for buildings, Brussels, Belgium, (2004).
[6] E.O.L. Lantsoght, C. van der Veen, A. de Boer, Proposal for the fatigue strength of concrete under cycles of compression, Construction and Building Materials, 107 (2016) 138-156.
[7] M.K. Lee, B.I.G. Barr, An overview of the fatigue behaviour of plain and fibre reinforced concrete, Cement and Concrete Composites, 26 (2004) 299-305.
[8] S. Korte, V. Boel, W. De Corte, G. De Schutter, Behaviour of fatigue loaded self-compacting concrete compared to vibrated concrete, Structural Concrete, 15 (2014) 575-589.
[9] C. Gaedicke, J. Roesler, S. Shah, Fatigue crack growth prediction in concrete slabs, International Journal of Fatigue, 31 (2009) 1309-1317.
[10] R. François, S. Laurens, F. Deby, Corrosion and its Consequences for Reinforced Concrete Structures, ISTE Press - Elsevier, 2018.
[11] S. Bhalla, N. Kaur, Prognosis of low-strain fatigue induced damage in reinforced concrete structures using embedded piezo-transducers, International Journal of Fatigue, 113 (2018) 98-112.
[12] A. Baktheer, J. Hegger, R. Chudoba, Enhanced assessment rule for concrete fatigue under compression considering the nonlinear effect of loading sequence, International Journal of Fatigue, 126 (2019) 130-142.
[13] F. Erdogan, G.C. Sih, On the Crack Extension in Plates Under Plane Loading and Transverse Shear, Journal of Basic Engineering, 85 (1963) 519-525.
[14] G.C. Sih, Strain-energy-density factor applied to mixed mode crack problems, International Journal of Fracture, 10 (1974) 305-321.
[15] D.J. Smith, M.R. Ayatollahi, M.J. Pavier, The role of T-stress in brittle fracture for linear elastic materials under mixed-mode loading, Fatigue & Fracture of Engineering Materials & Structures, 24 (2001) 137--150.
[16] M.R. Ayatollahi, M. Rashidi Moghaddam, F. Berto, T-stress effects on fatigue crack growth – Theory and experiment, Engineering Fracture Mechanics, 187 (2018) 103-114.

[17] M.L. Williams, On the Stress Distribution at the Base of a Stationary Crack, Journal of Applied Mechanics, 24 (1956) 6.

[18] H. Tada, P.C. Paris, G.R. Irwin, American Society of Mechanical Engineers., ASM International., The stress analysis of cracks handbook, 3rd ed., ASME Press : Professional Engineering Pub. : ASM International, New York, 2000.

[19] Y. Murakami, Stress intensity factors handbook. Volume 2 Volume 2, Pergamon Press, Oxford [Oxfordshire]; New York, 1987.

[20] C. Atkinson, R.E. Smelser, J. Sanchez, Combined mode fracture via the cracked Brazilian disk test, International Journal of Fracture, 18 (1982) 279-291.

[21] M. Abshirini, N. Soltani, P. Marashizadeh, On the mode I fracture analysis of cracked Brazilian disc using a digital image correlation method, Optics and Lasers in Engineering, 78 (2016) 99-105.

[22] M. Moazzami, M.R. Ayatollahi, H.R. Chamani, M. Guagliano, L. Vergani, Determination of higher order stress terms in cracked Brazilian disc specimen under mode I loading using digital image correlation technique, Optics & Laser Technology, 107 (2018) 344-352.

[23] M.R. Ayatollahi, M. Nejati, An over-deterministic method for calculation of coefficients of crack tip asymptotic field from finite element analysis, Fatigue & Fracture of Engineering Materials & Structures, 34 (2011) 159-176.

[24] M.R. Ayatollahi, M.R.M. Aliha, On the use of Brazilian disc specimen for calculating mixed mode I-II fracture toughness of rock materials, Engineering Fracture Mechanics, 75 (2008) 4631-4641.

[25] S. Seitl, P. Miarka, V. Bílek, The mixed-mode fracture resistance of C 50/60 and its suitability for use in precast elements as determined by the Brazilian disc test and three-point bending specimens, Theoretical and Applied Fracture Mechanics, 97 (2018) 108-119.

[26] T. Fett, Stress intensity factors and T-stress for internally cracked circular disks under various boundary conditions, Engineering Fracture Mechanics, 68 (2001) 1119-1136.

[27] P.S. Leevers, J.C. Radon, Inherent stress biaxiality in various fracture specimen geometries, International Journal of Fracture, 19 (1982) 311-325.

[28] Z. Knésl, K. Bednář, Two parameter fracture mechanics: calculation of parameters and their values, in, IPM of AS of Czech Republic, 1997.

[29] B. Yang, K. Ravi-Chandar, Evaluation of elastic T-stress by the stress difference method, Engineering Fracture Mechanics, 64 (1999) 589-605.

[30] R.J. Sanford, J.W. Dally, A general method for determining mixed-mode stress intensity factors from isochromatic fringe patterns, Engineering Fracture Mechanics, 11 (1979) 621-633.

[31] P. Miarka, A.S. Cruces, S. Seitl, L. Malíková, P. Lopez-Crespo, Influence of the constraint effect on the fatigue crack growth rate in S355 J2 steel using digital image correlation, Fatigue & Fracture of Engineering Materials & Structures, n/a (2020).

[32] V. Bilek, F. Khestl, P. Mec, Hybrid cements with non silicate activators, in: Solid State Phenomena, 2017, pp. 30-34.

[33] K.P. Vishalakshi, V. Revathi, S. Sivamurthy Reddy, Effect of type of coarse aggregate on the strength properties and fracture energy of normal and high strength concrete, Engineering Fracture Mechanics, 194 (2018) 52-60.

[34] B.L. Karihaloo, P. Nallathambi, Effective crack model for the determination of fracture toughness (KIce) of concrete, Engineering Fracture Mechanics, 35 (1990) 637-645.

[35] Y. Jenq, S.P. Shah, Two parameter fracture model for concrete, Journal of engineering mechanics, 111 (1985) 1227-1241.

[36] A. Spagnoli, A. Carpinteri, D. Ferretti, S. Vantadori, An experimental investigation on the quasi-brittle fracture of marble rocks, Fatigue & Fracture of Engineering Materials & Structures, 39 (2016) 956-968.

[37] M.R.M. Aliha, M. Sistaninia, D.J. Smith, M.J. Pavier, M.R. Ayatollahi, Geometry effects and statistical analysis of mode I fracture in guiting limestone, International Journal of Rock Mechanics and Mining Sciences, 51 (2012) 128-135.

[38] M.A. Sutton, J.J. Orteu, H. Schreier, Image Correlation for Shape, Motion and Deformation Measurements - Basic Concepts,Theory and Applications | Michael A. Sutton | Springer, Springer US, 2009.

[39] M. Mokhtarishirazabad, P. Lopez-Crespo, B. Moreno, A. Lopez-Moreno, M. Zanganeh, Optical and analytical investigation of overloads in biaxial fatigue cracks, International Journal of Fatigue, 100 (2017) 583-590.
[40] P. López-Crespo, R.L. Burguete, E.A. Patterson, A. Shterenlikht, P.J. Withers, J.R. Yates, Study of a Crack at a Fastener Hole by Digital Image Correlation, Experimental Mechanics, 49 (2009) 551-559.
[41] M. Mokhtarishirazabad, P. Lopez-Crespo, M. Zanganeh, Stress intensity factor monitoring under cyclic loading by digital image correlation, Fatigue & Fracture of Engineering Materials & Structures, 41 (2018) 2162-2171.
[42] S. Seitl, L. Malíková, V. Růžička, B. Moreno, P. Lopez-Crespo, Williams' expansion-based approximation of the displacement field in an Al 2024 compact tension specimen reconstructed from optical measurements, Fatigue & Fracture of Engineering Materials & Structures, 41 (2018) 2187-2196.
[43] G.R. Irwin, Plastic Zone Near a Crack and Fracture Toughness., in: Sagamore Research Conference, 1961, pp. 63-78.
[44] T.L. Anderson, Fracture mechanics: fundamentals and applications, CRC press, 2017.
[45] Matlab, version 9.10.0 (R2018a), The MathWorks Inc., 2018.
[46] P. Lopez-Crespo, A. Shterenlikht, E.A. Patterson, J.R. Yates, P.J. Withers, The stress intensity of mixed mode cracks determined by digital image correlation, Journal of Strain Analysis for Engineering Design, 43 (2008) 769-780.
[47] P. Lopez-Crespo, A. Shterenlikht, J.R. Yates, E.A. Patterson, P.J. Withers, Some experimental observations on crack closure and crack-tip plasticity, Fatigue & Fracture of Engineering Materials & Structures, 32 (2009) 418-429.
[48] M. Zanganeh, P. Lopez-Crespo, Y.H. Tai, J.R. Yates, Locating the Crack Tip Using Displacement Field Data: A Comparative Study, Strain, 49 (2013) 102-115.
[49] M. Azadi, M. Saeedi, M. Mokhtarishirazabad, P. Lopez-Crespo, Effects of loading rate on crack growth behavior in carbon fiber reinforced polymer composites using digital image correlation technique, Composites Part B: Engineering, 175 (2019) 107161.
[50] *Vic-2D V6 Reference Manual,*

Correlated Solutions Incorporated (C.S.Inc), in.
[51] *ANSYS® Academic Research Mechanical, Release 19.1*, in, 2018.
[52] A.P. Kfouri, Some evaluations of the elastic T-term using Eshelby's method, International Journal of Fracture, 30 (1986) 301-315.
[53] J.R. Rice, A Path Independent Integral and the Approximate Analysis of Strain Concentration by Notches and Cracks, Journal of Applied Mechanics, 35 (1968) 379-386.
[54] P. Miarka, S. Seitl, V. Bílek, Mixed-mode fracture analysis in high-performance concrete using a Brazilian disc test, Materiali in Tehnologije, 53 (2019) 233-238.